

A Metallographic Examination into Fatigue Crack Initiation and Growth in Ferrous PM Materials

Thomas F. Murphy, Bruce A. Lindsley, & Christopher T. Schade
Hoeganaes Corporation
Cinnaminson, NJ

Abstract

Porous materials behave differently under fatigue loading compared with pore-free materials. The internal free surfaces, i.e., pore edges, often act as crack initiation sites and cracks usually grow from one pore to a near-neighbor pore. Depending on the type of fatigue loading, this may occur simultaneously at multiple sites inside the part until the critical crack length is reached and fast fracture takes place. The phenomenon of crack initiation and growth will be explored using axial fatigue specimens tested to failure and where the load was removed prior to failure. The samples are pearlitic, nearly eutectoid, and in the as-sintered condition, having differences in both chemical composition and pearlite spacing. Furthermore, an additive was utilized to create larger pores in the sintered samples and allow the effect of pore size to be studied as it related to cyclic loading. Both light optical and scanning electron microscopy were used to examine the pore size distributions, interlamellar pearlite spacings, details on fracture surfaces, fracture surface profiles, and cross-sections through stressed regions in failed and pre-failure specimens.

Introduction

The features observed in a metallographic examination of powder metallurgy (PM) materials reveal several important characteristics that are unique to porous products. Because of these peculiarities, PM materials behave differently when subjected to various types of stress. The most obvious is the pore structure, which is a by-product of the press and sinter process. This structure is often interconnected and provides a large amount of internal surface area that is important in surface-sensitive applications, such as those experienced by a part subjected to cyclic loading.¹⁻³ This inherent pore structure acts as resident defects and has a profound effect on material behavior considering fatigue cracks usually initiate at

surface regions. In addition, the large pores and their frequently irregular shapes are often among the most important features within the microstructure regarding dynamic performance of a material. The large pores are most likely the largest defects in the material volume and their angular shapes often act as stress raisers that can promote crack initiation and growth.⁴⁻⁹ In these porous materials, once a crack has initiated, it usually grows from pore to pore.^{2,10,11}

Holes (pores) are important, not only in PM materials, but also in wrought alloys since they act as stress concentrators and can lead to crack initiation, growth, and eventual part failure. Although wrought materials are thought to be pore free, holes are formed when a part is subjected to fatigue cycling and some of the non-metallic inclusions are affected by the stresses. In particular, hard Al_2O_3 inclusions may debond from the surrounding metal and form a hole. With other hard inclusions where debonding does not take place, the inclusion may undergo cracking and then separate from the matrix. In both cases, the result is the creation of a hole in the interior of the part with an increase in the internal surface area. It is from these holes that cracks can initiate.³

With crack initiation being highly surface related and PM materials having a large amount of internal and external free surfaces, multiple cracks can start and grow simultaneously. As individual cracks grow, they proceed to link neighboring pores, enlarging the defect sizes through the combination of the crack lengths and the joined pore diameters. The load bearing cross-section of the matrix progressively lessens until a sufficient number of individual cracks and pores join and the final fracture occurs. If many cracks are formed through the material volume, the final fracture surface is often more irregular in appearance and shows a more tortuous profile. This situation occurs, not only in PM materials, but also in wrought samples where cracks can initiate at multiple sites prior to the final fracture.¹² Several cracks grow until either they join or the amount of intact material is reduced to the extent that it can no longer support the applied stress. In the case where fewer cracks initiate, crack growth and final fracture occur almost simultaneously. This type of fracture surface will be flatter and have a less irregular profile.

Alloying is another area where the PM techniques are unique compared with those practiced with other materials. In the method used most frequently, base iron or low-alloy steel powders are mixed with elemental, ferroalloy, or more complex particulate additives. The choice of additives usually has pronounced effects on the microstructure. In some cases, the additives alloy through solid state diffusion while others form a liquid phase during sintering and diffuse along particle edges while in the molten state. The resulting part volume is often not chemically homogeneous due to variability in diffusion caused by diffusion rates, internal surface area, particle sizes, etc. As a result of this heterogeneous alloy distribution, a variety of transformation products can form due to localized differences in material hardenability. Consequently, the combination of properties, both physical and mechanical, and the material response to the applied stresses may also be variable locally.

Additives can also alter the behavior of the material during the sintering process and change characteristics of the microstructure, such as grain size, precipitation behavior, interlamellar pearlite spacing, etc. The silicon and vanadium used in this study were selected because they have been shown to refine the spacing in a pearlitic microstructure and inhibit the precipitation of grain boundary carbides in hypereutectoid steels.^{25,26}

Furthermore, modifying sintering conditions can result in multiple changes to the microstructure. Raising the sintering temperature from the standard 1120 °C improves particle bonding, reduces surface area of

the internal porosity, and increases diffusion of the alloying additives. In addition, adjusting the cooling rate can change the combination of transformation products that are formed and possibly the scale of the microstructure.

Experimental Procedure

Specimen Preparation

The fatigue testing program was performed in two stages. Initially, three near-eutectoid alloy mixtures incorporating standard premix additives were evaluated to determine the effects of interlamellar pearlite spacing and ferrite composition on axial fatigue performance. These mix compositions were: F-0008 (Ancorsteel[®] 1000B + 0.8 w/o Asbury 3203H graphite), FC-0208 (Ancorsteel 1000B + 2 w/o ACuPowder 8081 Cu + 0.8 w/o graphite), and a patent pending steel microalloyed with silicon and vanadium (Ancorsteel 1000B + a proprietary additive system containing silicon and vanadium + 1.1 w/o graphite). Additionally, Acrawax C was used in all mixes as the lubricant. Transverse rupture strength (TRS), tensile, impact, and axial fatigue bars were pressed from these mixtures to green densities sufficient to achieve a 7.0 g/cm³ density after sintering. Both the carbon contents and green densities of the F-0008 and FC-0208 materials were altered slightly to account for the expected effects of two sintering temperatures. Constant sintered densities and carbon contents were desired in this study to eliminate contributions from those variables to the relative strengths.¹¹

Two compositions from the first stage, the F-0008 and the Fe-Si-V-C microalloyed steel, were the subjects of the second set of tests. The objective in this round of the testing was to examine the effect on axial fatigue performance of a larger pore size distribution. Changing the size of the pores was accomplished by altering the additives to the mix compositions; using additives that occupy space in the green bars, then burn-out during sintering. In both mixtures, the lubricant was changed to a combination of Kenolube plus an additional lubricant that was ground to a coarser particle size distribution and screened to remove the fine particles. The remaining coarse particles were added to each mix and, after sintering, provided the large pores. All other additives remained the same.

The F-0008 and FC-0208 samples were sintered in an Abbott belt furnace at 1120 °C (2050 °F) and 1260 °C (2300 °F) in a 90/10 nitrogen/hydrogen atmosphere. In Stage 1 of the program, they were cooled at two rates, approximately 0.4 °C/sec and 2.2 °C/sec. In Stage 2, only the faster cooling rate was used for the F-0008. The Fe-Si-V-C bars were processed at only the higher sintering temperature using the same Abbott furnace, but cooled with the two cooling rates in the first stage and only the faster cooling rate in the second stage. When the two cooling rates were used, the intention was to provide a difference in pearlite spacing within each material/sintering temperature group. The appropriate mechanical properties, hardness, and dimensional values were determined for each sintered bar. After mechanical and physical testing, specimens were selected for metallographic analysis.

Axial fatigue tests were carried out using unnotched, as-sintered bars with a continuous radius between the ends and a rectangular cross-section. The tests were run at a frequency of 60 Hz and a stress ratio of $R = -1$. Sufficient samples were run to provide data for development of the SN curves. From these tested samples, several were selected for metallographic examination.

Metallographic Analysis

Cross-sections were removed from broken TRS and fatigue bars to examine the overall microstructure, evaluate the pore structure, and measure interlamellar pearlite spacing. Pore size and shape distributions were measured, along with counting the number of pores in the prepared cross-sections from the faster cooled samples in each material/sintering temperature combination. Additionally, the pearlite spacing was measured on bars from each sintering condition using the image analysis (IA) system on secondary electron images (SEI) acquired using the scanning electron microscope (SEM). An examination of failed fatigue bars was performed on both the fracture surfaces and on sections taken transverse to the fractures. In some cases the surface details on the transverse cross-sections were protected through deposition of an electroless nickel plating before sectioning. Metallographic preparation of the cross-sections was performed using normal laboratory procedures with the addition of epoxy impregnation to aid in the correct characterization of the pore structure where necessary. Polished specimens were examined in both the as-polished and etched conditions. The specific etchant compositions will be described in later figures.

Pore analysis of the faster-cooled unetched sections was performed using an automated IA system. Pore size distribution was based on the cross-sectional area of the individual pores and the shape of each pore was determined using the expression:

$$4\pi A/P^2$$

where A is the cross-sectional area of an individual pore and P is the perimeter. For shape comparison purposes, a circle has the value of 1 and any shape with a longer perimeter for a given area (more irregular) will be <1. Through examination of the shape function, the estimated shape value is heavily dependent on perimeter length of a feature. At shape factor values <0.15, large changes in the perimeter length result in relatively small changes in the calculated shape value. The opposite is true at values >0.15, where comparatively small changes in perimeter length result in large changes in shape factor. In determining the shape distribution of the examined pore population, all pores having a maximum Feret diameter (caliper length) <6 μm were eliminated from the distribution. Approximately 50% of the measured pores in each sample were in this <6 μm size class and including this large number of small, regularly shaped pores in the overall analysis would skew the distribution toward higher shape values and provide a misleading description of the effects of sintering and alloying. However, these small pores were included in the size distribution and in field-based density estimates.

Image analyses of the individual pores used systematic sampling of the prepared cross-sections to ensure all areas of the cross-sections were evaluated. In total, 240 fields were examined on each sample surface with a total area of approximately 30 mm^2 per sample. Image resolution was 0.345 $\mu\text{m}/\text{pixel}$ with an overall pixel array of 1608 x 1212. The total number of pores measured in the size distributions ranged from 40,000 to 60,000 and the number included in the shape analyses was roughly 20,000 to 30,000; approximately half the number of pores examined in each sample. This variation in counted pores within each test was due to the characteristics of the different materials and their response to sintering. An estimation of the sintered density was made using all pores from the size distribution. The area fraction of the pores was converted to sectional density using 7.87 g/cm^3 as the pore-free density. These values

were compared with immersion density measurements made on entire sintered bars. The IA estimate was within an average of 0.05 g/cm³ of the immersion measurement.

The SEM was used for the examination of the fracture surfaces, cross-sections through the fractures, and to acquire the images for measurement of the pearlite spacing. Both secondary and backscattered electron images (BEI) were used where appropriate. Light optical microscopy (LOM) was used for the pore evaluations in the unetched condition while the samples were etched using combinations of nital and picral for general metallographic analysis and the pearlite spacing measurements. The procedure used to estimate the interlamellar pearlite spacing was described in the summary of Stage 1 testing.¹¹

Results and Discussion

As mentioned earlier, the pore structure^{4-9,17,18} and interlamellar pearlite spacing^{11,12,19-21} have been identified as major contributors to material properties and consequently, were a large part of this study. The evaluation of each will be discussed separately along with an examination of the characteristics on the fatigue fractures, both as projected images and in cross-section. In closing, after discussion of the microstructures and material behavior, a brief summary of the fatigue performance will be included.

The intent of the large pore samples was to determine the effect of the large pores/defects on the fatigue strength of the two materials. The FC-0208, which was tested in the initial stage of this program, was omitted from this more recent testing because those samples contained large pores from the addition of elemental copper.

Pore Analysis

The pores in the metallographically prepared cross-sections from failed fatigue bars were examined using the automated IA system for size and shape distribution and also their respective numbers. Sintered density of each material was relatively consistent at approximately 7.0 g/cm³. The emphasis in this testing was to describe the number, size, and shape of the large pores. Table 1 shows the comparison of the largest pore sizes, as determined by maximum length, in both phases of testing. The values in the table are totals from examination of the 30 mm² and all were from the samples cooled at the faster rate.

The data are separated into total counts, size as measured by maximum length, and shape results as described earlier. Each row represents a material composition and sintering temperature combination. The first five rows are results from the initial stage of testing and the final three are from the samples containing the coarse ground lubricant. The numbers of pores >6 μm are all within the 20,000 to 30,000 range. In each case where two sintering temperatures were used, the number from the higher temperature is lower compared with the lower temperature. Interestingly, where the large pores were created in the second round of testing to simulate the Cu-steel pore structure, the number of pores >6 μm in the large pore (LP) Fe-Si-V-C sample fits well with the FC-0208 material from the first round of testing.

The large pore counts were broken into two size groups and it is clear the objective of creating large pores by adding a coarse lubricant was successful. The largest size class increased in all instances and only the F-0008 1260 °C sample had slightly fewer pores >100 μm in length. Nevertheless, the number of large pores in the FC-0208 is still considerably higher than all other samples. A visual example of the pore sizes in the normal and LP size distribution samples is shown in Figure 1. The material is Fe-Si-V-C,

which has the fewest large pores in the normal sample, but shows a considerable increase with the addition of the coarse lubricant particles. Although the two samples were virtually the same in sintered density, the normal pore size distribution sample had more pores with a smaller average pore size, while the LP sample contained fewer pores, but with a larger pore size distribution.

Table 1. Image Analysis Results of the Pore Structure

Composition	Sintering Temp. (°C)	Number of Pores			50 Largest Pores	
		>6 μm	>100 μm	>150 μm	Average Circularity	Perimeter Change
Stage 1 – Normal Pore Size Distribution						
F-0008	1120	27,352	44	0	0.08	
F-0008	1260	24,689	52	1	0.11	
FC-0208	1120	23,212	121	12	0.13	
FC-0208	1260	21,821	144	9	0.13	
Fe-Si-V-C	1260	29,586	8	1	0.19	
Stage 2 – Large Pore Samples						
LP F-0008	1120	27,829	75	10	0.07	+7.0%
LP F-0008	1260	26,687	49	5	0.07	+20.2%
LP Fe-Si-V-C	1260	23,631	70	5	0.12	+25.6%

Considering circularity, only the 50 largest pore cross-sections were included in these calculations. Assuming the largest and most irregular defects are potentially the most harmful, these pores were separated from the total population for additional examination. In all three LP cases, the circularity was lower in comparison with the 50 largest pores from the normal pore size samples. Although the circularity values are only slightly lower, small changes at the low end of the 0 – 0.15 circularity range indicate relatively large changes in perimeter length, as described in the Experimental Procedure section. The far right column shows the increase in average perimeter length for the 50 largest pores in each material/sintering condition group. This increase in irregularity is attributed to the coarse lubricant particles and the fact that these large particles are softer than the metallic powders and therefore, no accommodation is made for them as the green compact is pressed. The lubricant particles deform and the resulting large pores shapes are defined by the surrounding metal particle edges.

Interlamellar Pearlite Spacing

The test method chosen to estimate the pearlite spacing in this study was described by Vander Voort and Roos¹³ and used by others¹⁴⁻¹⁶ to estimate the true mean spacing within the pearlitic microstructure. The

technique accounts for orientation differences in the pearlite caused by the sectioning plane through the sample cross-section and placement of the sample probes over the randomly oriented pearlite colonies.

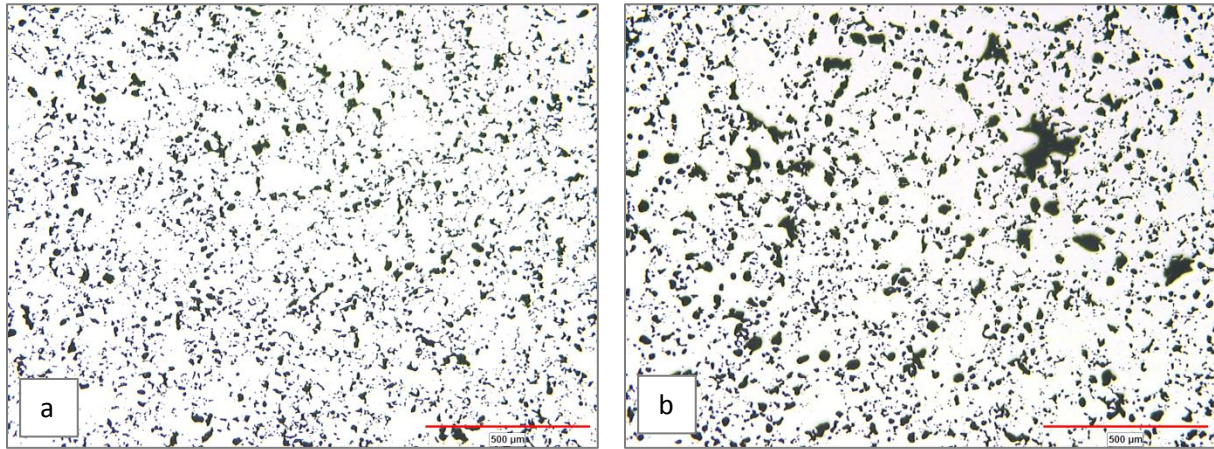


Figure 1. Images showing the relative pore sizes and shapes in the normal distribution (a) and the large pore sample (b). Both examples are from the Fe-Si-V-C material. LOM, Unetched

Figure 2 shows examples of pearlite from each of the three large pore samples. The images were taken at the same magnification to show the comparative differences in spacing. As can be seen in the F-0008 images, the higher sintering temperature yielded a finer spacing than the lower temperature. The Fe-Si-V-C material was, however, the finest of the group. In addition to the identification of each image in Figure 2, the pearlite spacing and etchant used are included in the caption.

Cracking and Fracture

The fracture surfaces of failed axial fatigue samples display features similar to those seen with failed wrought materials, i.e., dimpling, cleavage, fracture through pearlite colonies, etc. The major difference in appearance is that the edges of the pore network are also visible in the porous PM materials. The PM fatigue failures show a similar behavior observed with other PM failures where more pore surface is often visible on the fracture surface compared with the volume fraction of the porosity within the part.^{9,22-24} Evidently, the cyclic loading also seeks out the local 'weak' regions for initiation and growth of cracks. This may be especially apparent with axial fatigue where the tensile stresses are uniformly distributed across the material cross-section and not localized and directional as in bending fatigue.

It is apparent, however, that the method of failure is quite different. Where crack initiation of a wrought material is often located in a corner or near a surface and growth is nearly flat and radially shaped, the PM samples initiate numerous cracks throughout the material volume around the final crack. These cracks appear to originate at pore edges and travel from pore to pore, linking internal defects (pores), and creating larger discontinuities in the material volume than the pore network alone. They are also located in the material cross-section and not strictly at or near the outside surface of the sample.

Several samples were cycled at different stress levels for times estimated to initiate cracks but not cause failure. These samples were removed from the test equipment and sectioned in the stress direction prior to metallographic examination. Figures 3 and 4 show small cracks connecting or nearly connecting neighboring pores (indicated by arrows) before final failure of the sample. In Figure 4, it is unknown if

the upper crack was still growing toward the pore to the left when the load was removed because the local stresses would probably have been altered through linking of the pores by the lower crack.

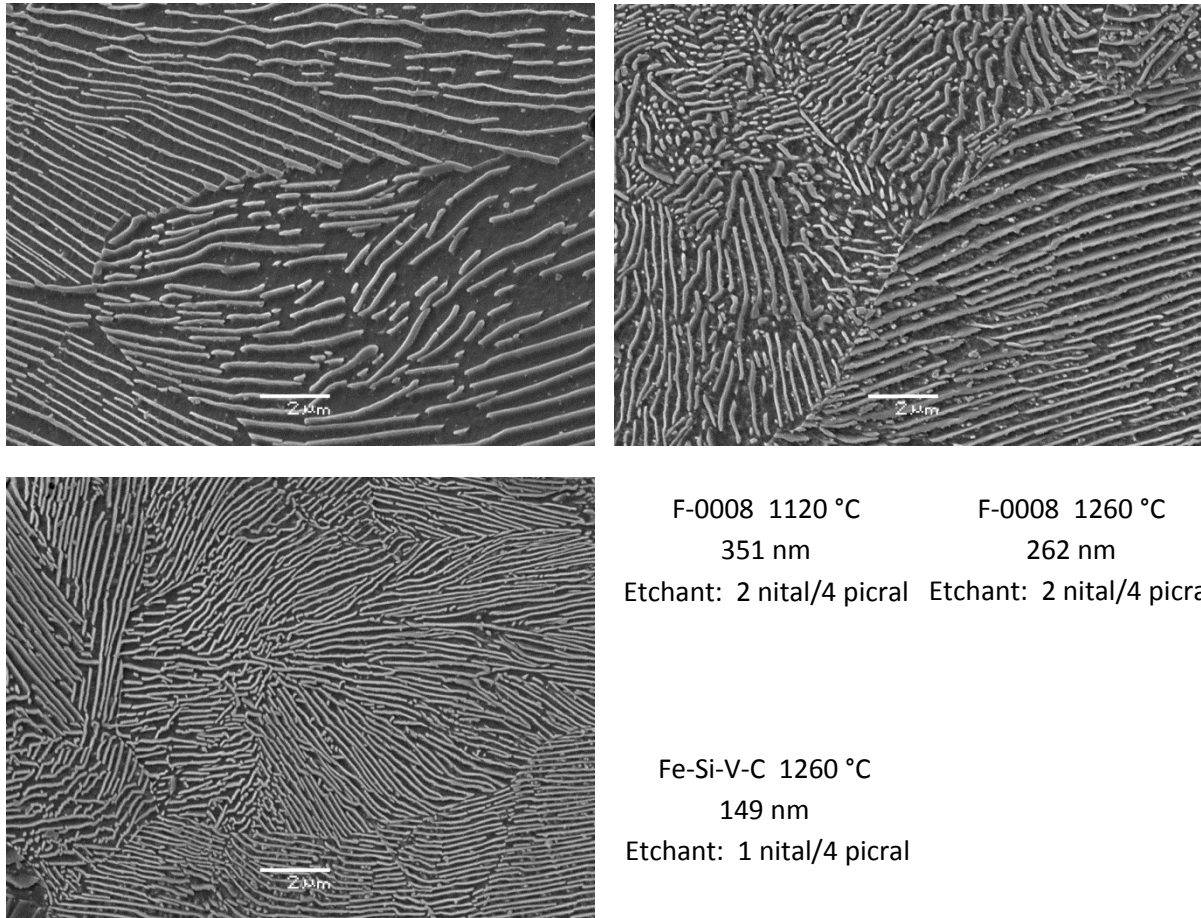


Figure 2. Examples of the pearlite microstructure in the three large pore samples. The interlamellar spacings and sample ID are shown in the insert along with the etchants. SEM-SEI

Figures 5 and 6 show examples of more extensive pre-failure cracking in a highly stressed sample. The sample contains a large pore located on the surface of the test bar, probably the result of the oversize lubricant addition. A crack is observed at the edge of the large pore extending, in this image, through six neighboring pores. The arrows indicate the crack path as it progressed from pore-to-pore. In a region approximately 50 μm vertical from this surface-connecting crack is another cluster of cracks (highlighted within the white oval) that does not intersect the surface in this plane of polish. As illustrated by the upper set of cracks, it is unusual for initiation and early growth to extend to the outside surface of the test piece. It appears that cracks usually start at a pore edge in the sample interior and grow radially, roughly perpendicular to the stress direction. An extension of the upper cracks from Figure 5 is seen in Figure 6, with the area to the left of the white dashed line showing the overlap in the two images. As seen in the locations of the cracks, they occasionally branch as they grow, connecting pores both above and below their horizontal location. It is unknown if the total length of this cracking is the result of crack growth from a single initiation source or if several cracks initiated, grew simultaneously, and joined to form

larger individual cracks. At this stage in the crack growth, the total depth of the damage from the surface is several hundred micrometres.

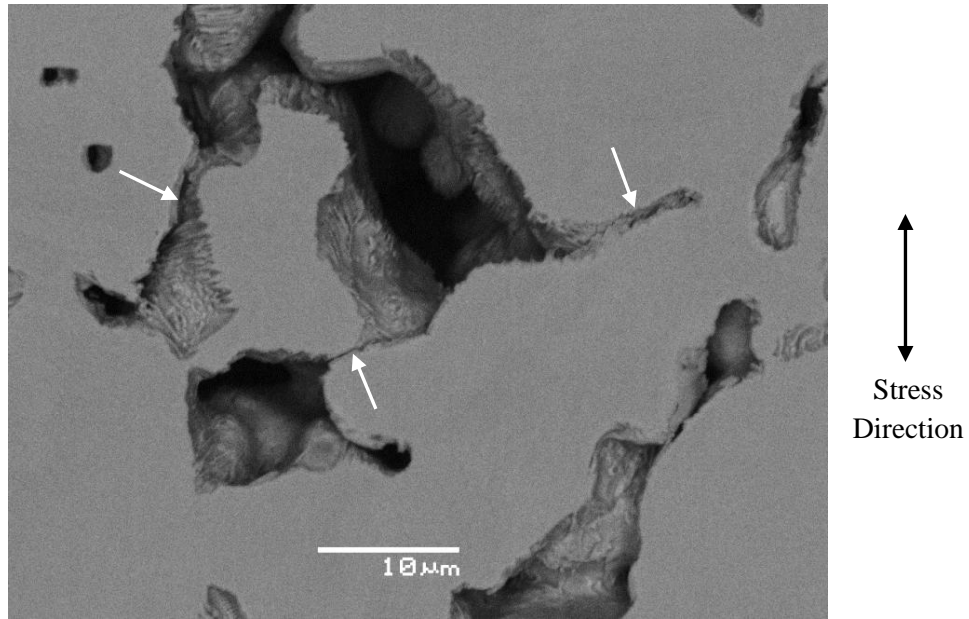


Figure 3. F-0008, 1120 °C sample with cracks linking or nearly linking neighboring pores.
SEM-BEI, Unetched

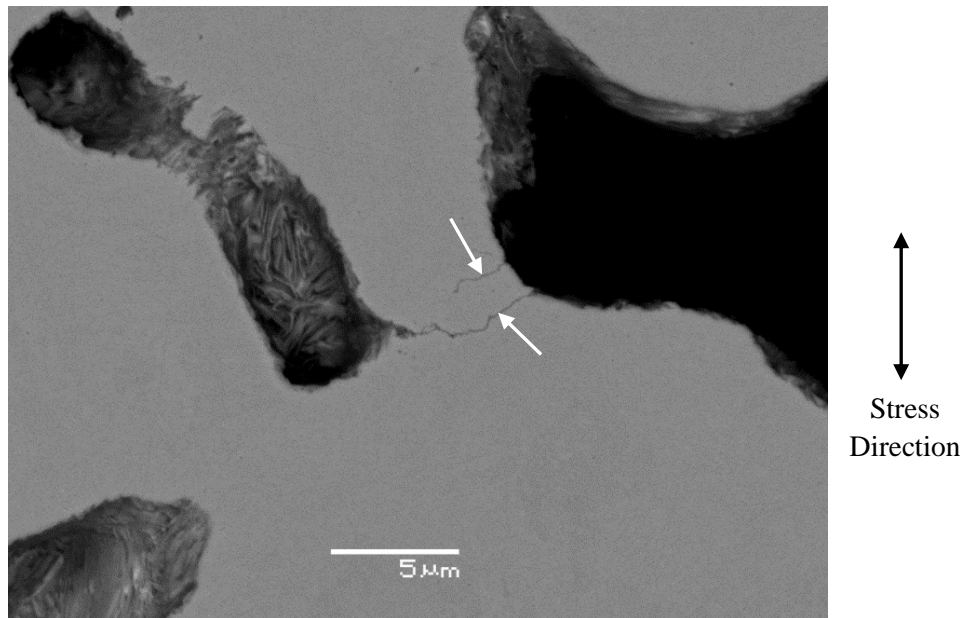


Figure 4. Fe-Si-V-C sample showing crack initiation and growth from pore-to-pore.
SEM-BEI, Unetched

The relationship of the cracks with the pearlitic microstructure is seen in Figures 7 and 8. These are locations within the white rectangles in Figure 6, with the annotated numbers corresponding to the figure numbers. In Figure 7, a crack can be seen at the edge of a pearlite colony (left), parallel to the lamellae

(middle), and transverse to the direction of the lamellae (right). The position of the crack in Figure 8 is basically across the pearlite colony. Part of the crack is at a sharp angle crossing the pearlite and part is nearly perpendicular to the direction of the colony. There does not seem to be a preferential location of the crack regarding the pearlitic microstructure. Rather, it appears the locations of the individual pores, local material strength, and stress concentrations at the crack tips are more important to crack growth.

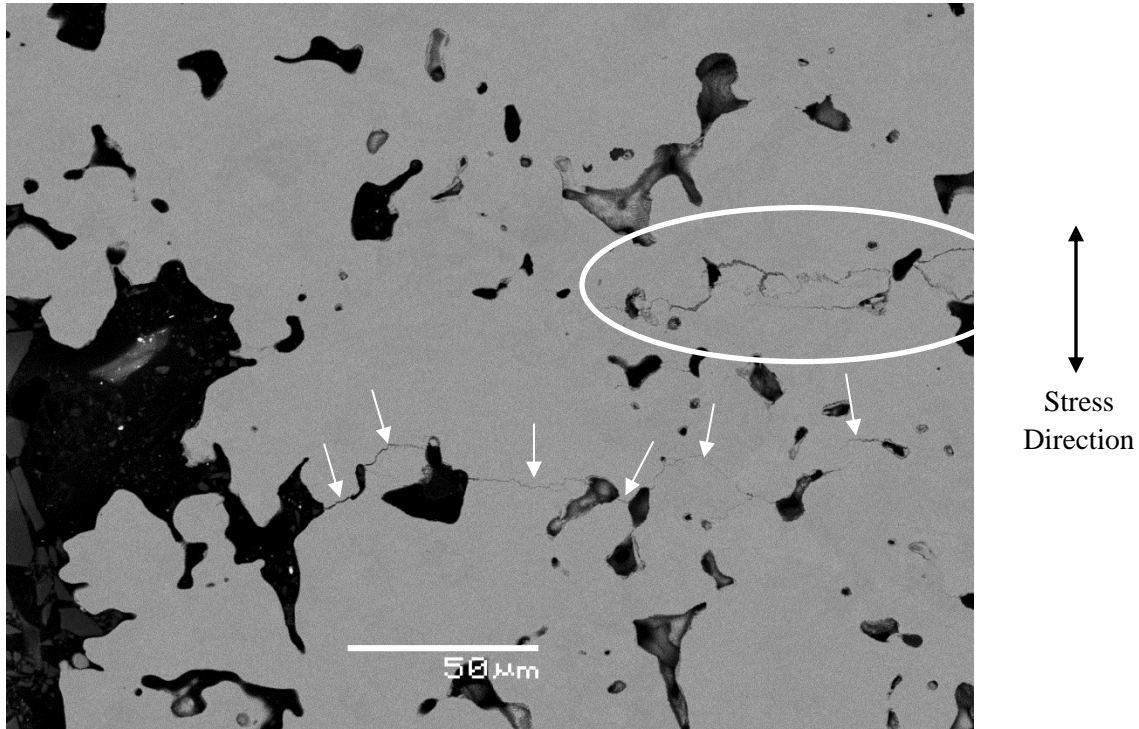


Figure 5. Pre-failure cracks found at a large pore on the surface of an F-0008, 1260 °C sinter sample. (The material to the left of the large pore is metallographic mounting material). SEM-BEI, unetched

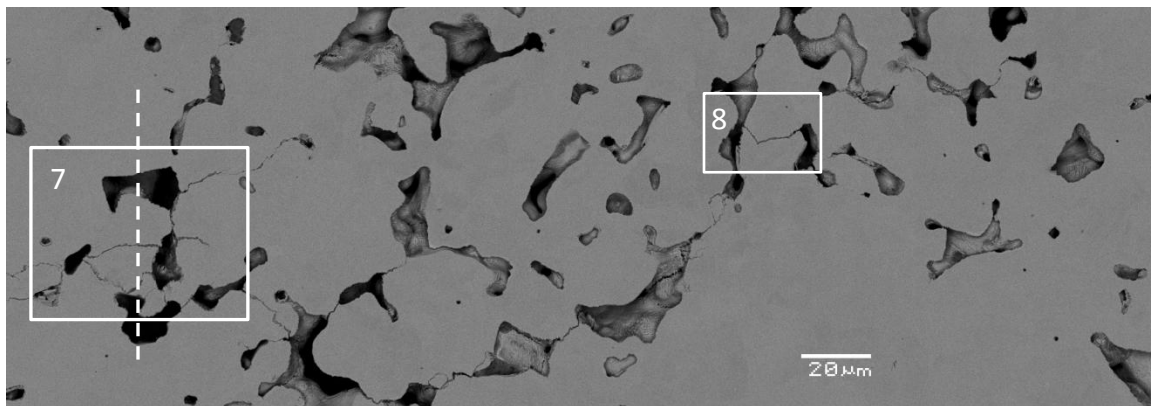


Figure 6. Extension of the upper crack shown in Figure 4 (F-0008, 1260 °C). Stress direction is vertical. SEM-BEI, unetched

The size, number, and locations of cracks appear to be related to the level of stress applied to the sample. In the examination of sections taken transverse to the fracture surface, higher stressed samples contained

more cracks not connected to the final fracture compared with samples tested at lower stress levels. They were also longer and distributed greater distances from the terminal crack, thus affecting a greater material volume. Conversely, cracks formed at lower stress levels seem to be less frequent, shorter, and found in the material closer to the final fracture. Specifically, in the Fe-Si-V-C material stressed at two levels, cracks were observed approximately 0.25 mm from the final fracture in the sample subjected to the low stresses while in a sample of the same material which had seen higher stresses, cracks were observed more than 2 mm from the final fracture. This indicates the surface regions (pore edges) may be variable in strength and the high stresses may affect more individual areas than the lower stresses making them more susceptible to cracking. Consequently, it appears cracks initiate and grow in more locations when highly stressed. This is illustrated in Figure 9, where Figure 9a shows a typical short crack in the Fe-Si-V-C material which had experienced lower stresses, while Figure 9b is the same material which has seen higher stresses and shows more extensive cracking. Special attention should be paid to the difference in magnification used for these images and the relative size of the pores and cracks.

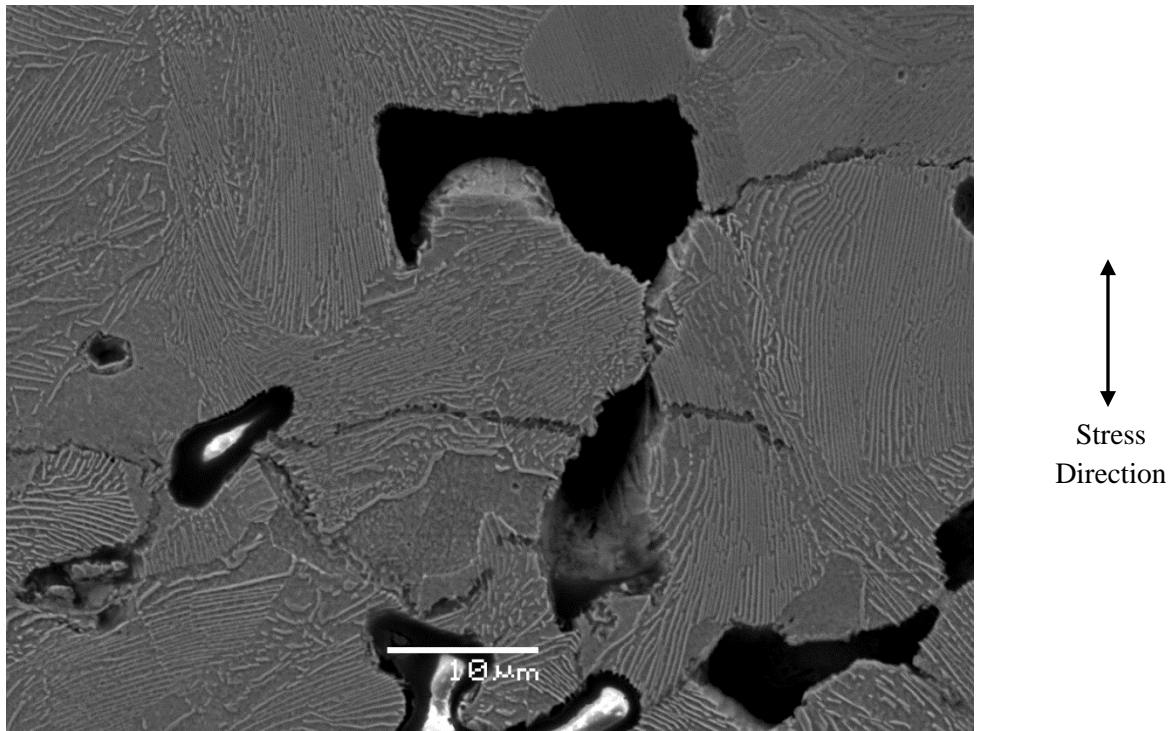


Figure 7. Detail from Figure 5 showing the crack location in the pearlitic microstructure.
SEM-SEI, etched using 2 nital/4 picral

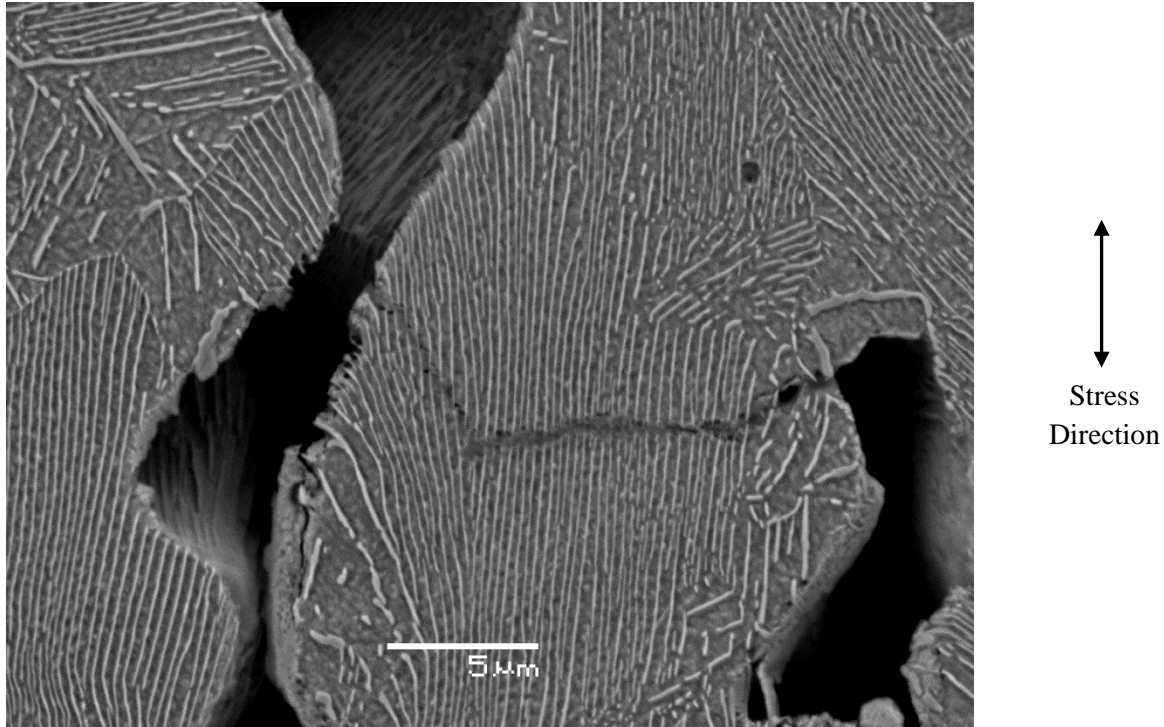


Figure 8. Detail from Figure 5 showing the crack location in the pearlitic microstructure.
SEM-SEI, etched using 2 nital/4 picral

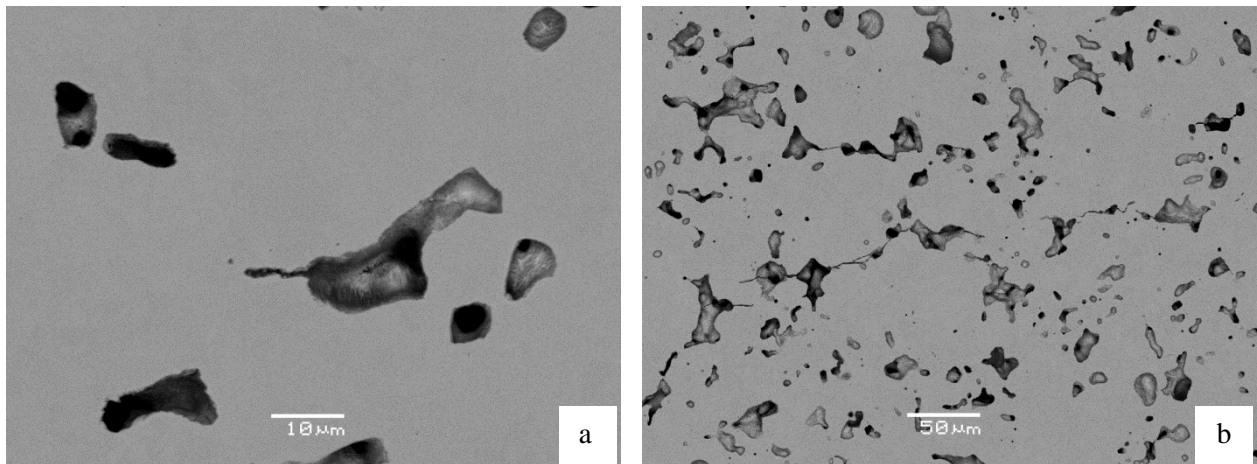


Figure 9. The Fe-Si-V-C material tested at two stress levels. Image 9a is the result of low stresses and 9b is from the higher stresses. Stress direction is vertical.
SEM-BEI, unetched

Another consequence of the variation in stress level is in how the final fracture is formed. As shown above, a greater number of cracks distributed over a larger material volume is the result of higher stresses, while the opposite is true of samples stressed at lower levels. In both cases the cracks grow until they reach pores and the process may start again with an additive increase in defect size. However, if more cracks are growing simultaneously through a larger material volume, as is the case with the higher stressed samples, the likelihood of linking to a pore already containing a crack is increased. As a result, the amount of material supporting the load is significantly reduced and the final fracture may result with a

more irregular fracture surface profile. Cross-sections through two fracture surfaces are seen in Figure 10. The surface of the higher stressed sample (Figure 10a) is substantially longer and more irregular than the surface of the lower stressed sample (Figure 10b). This indicates more pre-fracture cracking through a larger material volume in the higher stressed sample and a joining of the cracks as the sample failed.

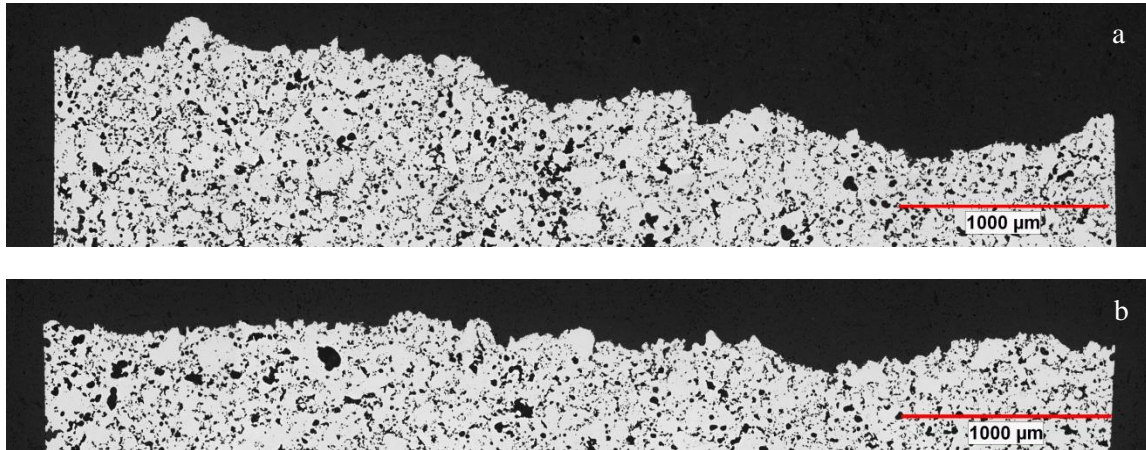


Figure 10. Transverse sections through fractures of the Fe-Si-V-C material stressed at two levels. Image 'a' is from the sample tested at the higher stress level and image 'b' was tested at lower stresses.
LOM, unetched

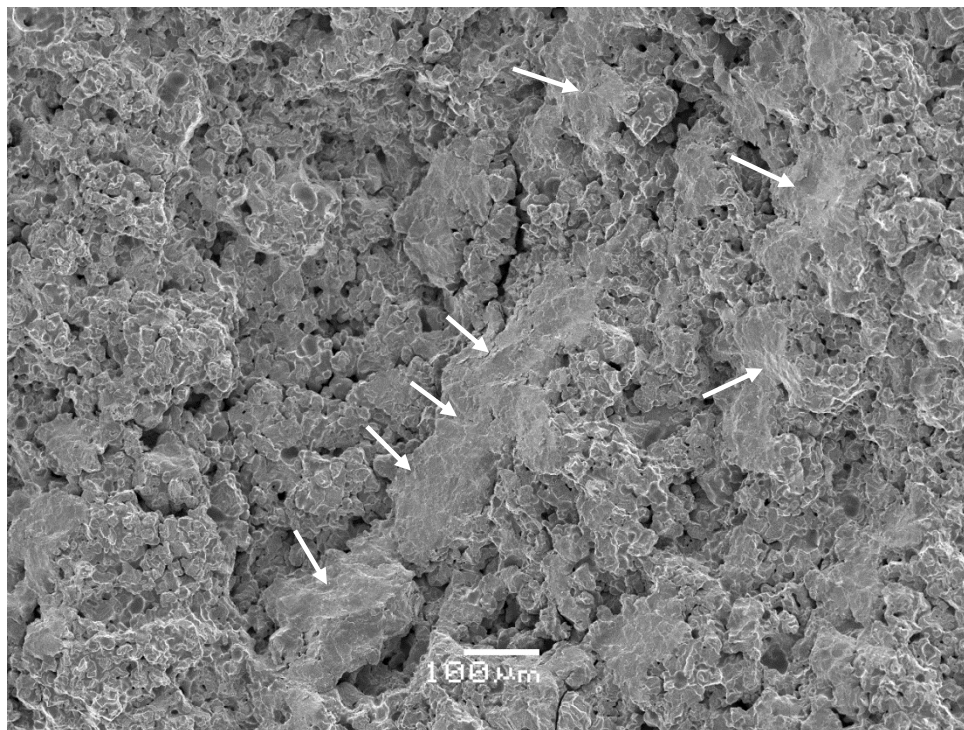


Figure 11. The fracture surface from a higher stressed Fe-Si-V-C sample. The rubbed regions are relatively flat and lack the details of normal fractures
SEM-SEI

An interesting feature was observed on the fracture surfaces, with examples emphasized in Figure 11 using arrows. Localized damage in the form of surface deformation was present in small regions and it is hypothesized they were among the first areas to fracture. Apparently, in the sequence of crack initiation and growth, these early internal cracks are surrounded with intact material that is capable of supporting the applied tensile loads. As cycling continues, the mating surfaces from these early cracks contact repeatedly, rub together, and obliterate all fracture characteristics and often the exposed pore surfaces. No damage is apparent on the surface details surrounding them as these regions had not yet cracked. These rubbed regions are scattered throughout the fracture surface, not limited to a certain crack face orientation, and were present in all samples. However, they were found more frequently on surfaces that were more irregular, such as the Fe-Si-V-C sample tested at the higher stress level.

An additional rubbed region is presented in Figure 12 where the amount of rubbing has caused flat, abraded metal flakes to form on the surface. This area is void of fracture details and all of the original pore edges have been completely filled with smeared metal. The areas in the lower right and upper left corners of the image show only fresh, undisturbed fracture.

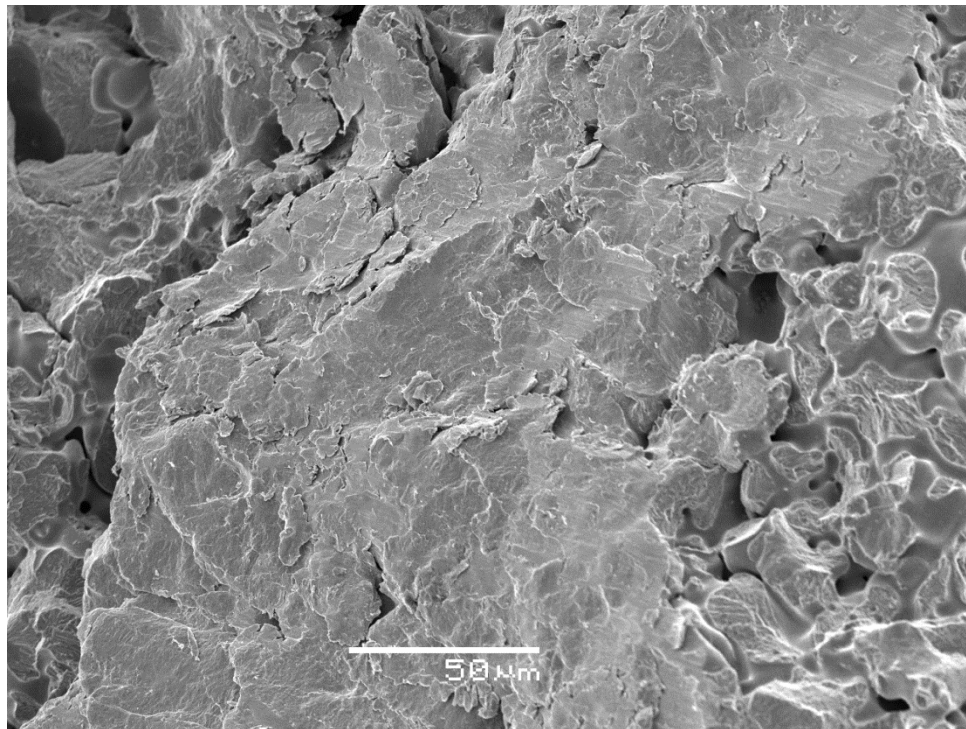


Figure 12. Area of a failed Fe-Si-V-C material showing the rubbed features.

SEM-SEI

Fatigue Performance

The fatigue endurance limits (FEL) of samples from both the normal and large pore size distributions are presented in Table 2.

**Table 2. Fatigue Performance
Normal Pore Size Distribution Samples vs. Large Pore Samples**

Material	Sintering Temperature (°C)	Pore Size Distribution	90% FEL MPa (psi)
F-0008	1120	Normal	110 (16,000)
F-0008	1120	Large	106 (15,400)
F-0008	1260	Normal	144 (20,900)
F-0008	1260	Large	121 (17,600)
Fe-Si-V-C	1260	Normal	197 (28,600)
Fe-Si-V-C	1260	Large	206 (29,900)

The data show that the large pores had a negligible effect on fatigue performance of the two materials. Where the effect was expected to be strongly negative, only the F-0008 exhibited a slight reduction in the FEL values. Conversely, the large pore Fe-Si-V-C material showed a modest improvement in performance compared with the normal pore size distribution samples. The similarity in results within each condition suggests the variability may be within experimental testing error.

A FEL improvement of nearly 50% was observed comparing the results of the Fe-Si-V-C steel and the F-0008. There are several reasons for this increase. They include alloying of the Si and V and the benefits of high temperature sintering with the faster cooling rate. As stated previously, the Si and V strengthen the ferrite within the pearlite colonies and inhibit the precipitation of carbides in the grain boundaries with hypereutectoid compositions. This allows the use of higher carbon contents and the transformation of more carbides in the pearlite without the normal embrittling effects usually seen with hypereutectoid carbon levels. High temperature sintering also improves sintering and oxide reduction, smooths pore surfaces, and enhances diffusion of the added alloying materials. The increased cooling rate refines the interlamellar pearlite spacing, which also results in a substantial improvement in FEL.

Conclusions

This metallographic analysis of axial-fatigue tested pearlitic PM steels has revealed several interesting results. While some are logical extensions of what has been found in wrought steels, others are unique to PM. In this study, all materials had a microstructure that was nearly eutectoid pearlite and all samples were sintered to nominally the same 7.0 g/cm³ density.

- With the increase in pore size distribution, the weaker iron-carbon F-0008 showed only minor decreases in the fatigue endurance limit at both sintering temperatures while the stronger, Fe-Si-V-C material showed no negative effects.
- The higher stress levels appear to create more pre-failure cracks compared with samples examined after being stressed at lower levels. These cracks were more numerous and showed more connection with neighboring pores.

- The extent of the cracks located in the regions surrounding the terminal crack were more frequent and extended farther into the sample volume with the higher stressed samples. Samples stressed at lower levels showed fewer cracks and their locations were substantially closer to the final fracture.
- The large pores did not appear to be the primary crack initiation sites. Most of the cracks observed in the pre-failure specimens appeared to originate at the smaller, normal size pores.
- Crack growth continued to be from pore-to-pore, regardless of the pore sizes in the vicinity.

Acknowledgements

The authors would like to thank Wing Hong Chen, Gerard Golin, Barry Diamond and Eric Alesczyk for their valuable assistance during various phases of this program and Dr. Brian James for his editorial and technical suggestions.

References

1. J.K. Nisbett & R.G. Budynas, *Shigley's Mechanical Engineering Design*, Eighth Edition, 2006, McGraw-Hill Primis, http://highered.mcgraw-hill.com/sites/0072520361/information_center_view0/primis_online.html
2. Hadrboletz & B. Weiss, "Fatigue Behaviour of Iron Based Sintered Material: A Review", *Int. Mats Rev*, 1997, vol. 42, no. 1, pp. 1-44
3. N.M.A. Eid & P.F. Thomason, "The Nucleation of Fatigue Cracks in a Low-Alloy Steel Under High-Cycle Fatigue Conditions and Uniaxial Loading", *Acta Met*, 1979, vol. 27, pp. 1239-1249.
4. P. Beiss and S. Lindlohr, "Porosity Statistics and Fatigue Strength of Sintered Iron", *Int. J. of Powder Met.*, 2009, vol. 45, no. 2, pp. 39-48.
5. P. Beiss and M. Dalgic, "Effect of Pore Structure on Bending Fatigue Strength of Sintered Steel", *Advances in Powder Metallurgy & Particulate Materials 1996*, compiled by T. Cadle and K.S. Narasimhan, Metal Powders Industries Federation, Princeton, NJ, 1996,
6. H. Danninger, D. Spoljaric, and B. Weiss, "Microstructural Features Limiting the Performance of PM Structural Parts", *Advances in Powder Metallurgy & Particulate Materials – 1996*, compiled by T. Cadle and K.S. Narasimhan, Metal Powders Industries Federation, Princeton, NJ, 1996, part 13, pp. 13-479 - 13-490.
7. H. Danninger & B Weiss, "High Cycle Fatigue of Powder Metallurgy Materials", *VIII Congreso Nacional de Propiedades Mecanicas de Solidos*, Editor: Vicente Amigo, Gandia, Espainia, 2002, pp. 195-204.
8. J. Polasik, J.J. Williams, N. Chawla, and K.S. Narasimhan, "Fatigue Crack Initiation and Propagation in Ferrous Powder Metallurgy Alloys," *Adv. Powder Metall. Part. Mater.*, compiled by W. Eisen and S. Kassam, (2001), vol. 10, Metal Powder Industries Federation, pp. 172-187.
9. H.E. Exner and D. Pohl, "Fracture Behavior of Sintered Iron", *Powder Metallurgy International*, 1978, vol. 10, no. 4 pp. 193-196.
10. J. Holmes & R.A. Queeney, "Fatigue Crack Initiation in a Porous Steel", *Powder Metallurgy*, 1985, vol. 28, no. 4, pp. 231-234.
11. T.F. Murphy, B.A. Lindsley, & C.T. Schade, "Effect of Pearlite Spacing and Chemical Composition on the Axial-Fatigue Behavior of Fully Pearlitic PM Steels: A Metallographic Study", *Int. J. Powder Met.*, 2012, vol. 48, no. 5, pp. 23-39.

12. G.T. Gray III, A.W. Thompson, & J.C. Williams, "Influence of Microstructure on Fatigue Crack Initiation in Fully Pearlitic Steels", *Met. Trans. A*, 1985, vol. 16A, pp. 753-760.
13. G.F. Vander Voort and A. Roosz, "Measurement of the Interlamellar Spacing of Pearlite", *Metallography*, 1984, vol. 17, no. 1, pp. 1-17.
14. E.E. Underwood, *Quantitative Stereology*, Addison-Wesley Publishing Co., Reading, MA, 1970.
15. J.F. Tilbury, T.D. Mottishaw, and G.D.W. Smith, "Measurements of the Spread in Pearlite Spacings", *Metallography*, 1986, vol. 19, no. 2, pp. 243-246.
16. N. Ridley, "A Review of the Data on the Interlamellar Spacing of Pearlite", *Met. Trans. A*, 1984, vol. 15A, pp. 1019-1036.
17. G.H. Gessinger, H. Metzler, F. Esper, and H.E. Exner, "Pore Geometry and Mechanical Properties of Sintered Iron and Steel", *Powder Metallurgy*, Third European Powder Metallurgy Symposium 1971, Institute of Metals, 1971, Conference Supplement 1, pp. 289-310.
18. N. Chawla, X. Deng, M. Marucci, and K.S. Narasimhan, "Effect of Porosity on the Microstructure and Mechanical Behavior of Powder Metallurgy Fe-Mo-Ni Steels", *Advances in Powder Metallurgy & Particulate Materials – 2003*, compiled by R. Lawcock and M. Wright, Metal Powder Industries Federation, Princeton, NJ, 2003, part 7, pp. 257-269.
19. J.M. Hyzak and M. Bernstein, "The Role of Microstructure on the Strength and Toughness of Fully Pearlitic Steels", *Met. Trans. A*, 1976, vol. 7A, pp. 1217-1224.
20. A.R. Marder and B.L. Bramfitt, "The Effect of Morphology on the Strength of Pearlite", *Met. Trans. A*, 1976, vol. 7A, pp. 365-372.
21. J. Toribio, B. Gonzalez, and J-C. Jatos, "Influence of the Microstructure of Eutectoid Steel on the Cyclic Crack Propagation: Pearlite and Spheroidite", *Int. J. Fract.*, 2011, vol. 171, no. 2, pp. 209-215.
22. H. Danninger, D. Spoljaric, G. Jangg, B. Weiss, and R. Stickler, "Characterization of Pressed and Sintered Ferrous Materials by Quantitative Fractography", *Praktische Metallographie*, 1994, vol. 31, no. 2, pp. 56-69.
23. T.F. Murphy and B. Lindsley, "Metallographic Analysis of PM Fracture Surfaces", *Advances in Powder Metallurgy and Particulate Materials – 2007*, compiled by J. Engquist and T.F. Murphy, Metal Powder Industries Federation, Princeton, NJ, 2007, part 11, pp. 1-15.
24. T.F. Murphy, "Evaluation of PM Fracture Surfaces Using Quantitative Fractography", *Int. J. of Powder Met.*, 2009, vol. 45, no. 2, pp. 49-61.
25. K. Han, D.V. Edmonds, and G.D.W. Smith, "Optimization of Mechanical Properties of High-Carbon Pearlitic Steels with Si and V Additions", *Met. & Mat. Trans. A*, 2001, vol. 32A, pp. 1313-1324.
26. K. Han, T.D. Mottishaw, G.D.W. Smith, D.V. Edmonds, and A.G. Stacey, "Effects of Vanadium Additions on Microstructure and Hardness of Hypereutectoid Pearlitic Steels", *Mat. Sci. & Eng. A*, 1995, vol. 190, pp. 207-214.